

Linear Canonical-Ensemble Quantum Monte Carlo: From Dilute Fermi Gas to Flat-Band Ferromagnetism

Tu Hong,¹ Kun Chen,^{2,*} and Xiao Yan Xu^{1,3,†}

¹*Key Laboratory of Artificial Structures and Quantum Control (Ministry of Education)
School of Physics and Astronomy, Shanghai Jiao Tong University, Shanghai 200240, China*

²*Institute of Theoretical Physics, Chinese Academy of Sciences, Beijing, China*

³*Hefei National Laboratory, Hefei 230088, China*

(Dated: January 21, 2026)

We present a finite-temperature canonical-ensemble determinant quantum Monte Carlo algorithm that enforces an exact fermion number and enables stable simulations of correlated lattice fermions. We propose a stabilized QR update that reduces the computational complexity from standard cubic scaling $O(\beta N^3)$ to linear scaling $O(\beta N N_e^2)$ with respect to the system size N , where N_e is the particle number. This yields a dramatic speedup in dilute regimes ($N_e \ll N$), opening unbiased access to large-scale simulations of strongly correlated low-density phases. We validate the method on the dilute Fermi gas with onsite Hubbard interactions, observing the suppression of the fermion sign problem in the dilute limit. Furthermore, we apply this approach to an one-dimensional flat-band system, where the canonical ensemble allows for precise control over filling. We reveal a ferromagnetic instability at low temperatures in the half-filling regime. Our linear-scaling approach provides a powerful tool for investigating emergent phenomena in dilute quantum matter.

Introduction— Low carrier density regimes of correlated electron systems host a variety of quantum phenomena driven by a common mechanism: the quenching of kinetic energy relative to Coulomb interactions. As the average interparticle spacing—captured by the dimensionless Wigner–Seitz radius r_s —increases, the collapsing Fermi energy ($E_F \propto n^{2/d}$) drives the system away from a simple Fermi liquid. In the clean continuum limit, this evolution produces enhanced effective masses, diverging spin susceptibilities, and ultimately Wigner crystallization at large r_s [1–5]. In complex material environments, such as dilute doped oxides and semiconductor heterostructures, the depressed Fermi energy often becomes comparable to phonon or dielectric modes. This breakdown of the adiabatic approximation facilitates unconventional superconducting phases that defy the standard BCS description, exhibiting non-monotonic critical temperature dependence and strong-coupling features [6–8]. Furthermore, in lattice systems where low filling coincides with narrow bandwidths or non-trivial topology—including Landau levels and moiré superlattices—the kinetic quenching is amplified by band geometry. This interplay can stabilize exotic phases ranging from fractional Chern insulators [9–14] to anomalous Hall crystals, where spontaneous symmetry breaking coexists with topological phase [15–19]. Collectively, these studies emphasize that interaction-driven ordering tendencies, whether in the continuum or on a lattice, are dramatically strengthened in the dilute limit, necessitating non-perturbative approaches to capture the competition between long-range correlations and quantum fluctuations.

From a computational standpoint unbiased finite-temperature determinant quantum Monte Carlo (DQMC), diagrammatic Monte Carlo, and related methods in this regime face the coupled challenges of

achieving fine-grained exact particle-number control at very low densities on feasible lattice sizes, mitigating the fermionic sign problem, and managing the steep growth of computational cost with system size and interaction strength [20–25]. Take the finite temperature DQMC as an example, the computational complexity is $O(\beta N^3)$, where N is the system size, and β is the inverse temperature. Numerous optimizations, including delay update [26], submatrix update [27] and self-learning updates [28–30], enhance performance but fail to alter this underlying scaling. While truncation algorithms can reach $O(\beta N N_e^2)$ [31, 32] (with particle number N_e), they introduce a systematic error that requires careful control. Therefore, developing an algorithm that is both unbiased and achieves sub-cubic scaling remains a central challenge in computational many-body physics.

Several studies have imposed the canonical ensemble in DQMC [33–38]. In parallel, other efforts have integrated real-space Fock state sampling into DQMC, primarily to enhance the efficiency of simulating cold-atom “snapshots” [39]. More recently, the Fock-State DQMC framework [40] was proposed, offering a new path by sampling both auxiliary fields and Fock-state configurations, which is highly flexible for imposing ensemble constraints. Crucially, however, all these approaches remain limited by the inherent cubic complexity.

In this work, we go beyond the conventional cubic scaling by introducing a numerically stable and efficient scheme to a canonical-ensemble constrained Fock-state DQMC [40], built upon a stabilized QR update algorithm [41]. This advance reduces the computational complexity from $O(\beta N^3)$ down to $O(\beta N N_e^2)$ while remaining numerically exact and unbiased. This advance enables large-scale and unbiased simulations of dilute systems, making direct validation of cold-atom experiments fea-

sible. Furthermore, because this efficient, fixed-particle framework is structurally similar to the projection version of DQMC, it seamlessly inherits the rich ecosystem of optimizations previously developed there, establishing it as a powerful, general and unbiased approach.

Ensemble constrained quantum Monte Carlo— We start with the partition function of the Hubbard model in the canonical ensemble using the Fock-state basis $|\eta\rangle = \prod_i (c_{i\uparrow}^\dagger)^{n_{i\uparrow}} (c_{i\downarrow}^\dagger)^{n_{i\downarrow}} |0\rangle$ [40]:

$$Z = \text{Tr}_\eta[e^{-\beta H}] = \sum_{\eta, \mathbf{s}} \det [P_\eta^\dagger B_\mathbf{s}(\beta, 0) P_\eta], \quad (1)$$

where P_η projects onto the occupied sites of configuration η , and $B_\mathbf{s}(\beta, 0) = \prod_{\ell=1}^{L_\tau} B_{\mathbf{s}_\ell}$ is the imaginary-time evolution matrix under auxiliary fields \mathbf{s} from a discrete Hubbard-Stratonovich transformation. The procedure for auxiliary-fields updates is similar to the projection version of DQMC, and the traditional fast update algorithm requires a computational complexity of $O(\beta N N_e^2)$ to update all space-time lattice points, while the newly developed delay update [27, 42] and submatrix algorithm [27] can further enhance the speed by leveraging computer cache.

However, EC-QMC introduces an additional Monte Carlo step for sampling Fock states. To implement the important sampling of Fock state, we need to calculate the ratio of weights when we propose the update $\eta \rightarrow \eta'$,

$$r = \frac{\det[P_{\eta'}^\dagger B_\mathbf{s}(\beta, 0) P_{\eta'}]}{\det[P_\eta^\dagger B_\mathbf{s}(\beta, 0) P_\eta]}. \quad (2)$$

To update the Fock state, a method proposed in Ref. [40] maintains a matrix which depends on the full matrix elements of $B_\mathbf{s}(\beta, 0)$. Because the matrix $B_\mathbf{s}(\beta, 0)$ is singular at low temperatures and needs to be calculated in a numerically stable way, the complexity of updating the Fock state is at least $O(\beta N^3)$, which is larger than the complexity for updating the auxiliary fields.

Linear ensemble constrained quantum Monte Carlo— To overcome the bottleneck in Fock state updates, we propose a stable QR update algorithm that reduces the computational scaling from cubic to linear, thereby establishing the Linear Ensemble Constrained Quantum Monte Carlo (LEC-QMC).

Any Fock state update involves particle removal and addition. While removing a particle is physically trivial—amounting to the deletion of existing data—its implementation is structurally involved, as it necessitates permuting the columns to reorganize the matrix. In contrast, adding a particle is algorithmically non-trivial: it requires calculating new imaginary-time evolution under the auxiliary field \mathbf{s} . Since the propagator $B_\mathbf{s}(\beta, 0)$ becomes singular at low temperatures, a direct calculation is unstable.

Previous algorithm implicitly relies on the full matrix $B_\mathbf{s}(\beta, 0)$ [40], which amounts to pre-calculate evolution

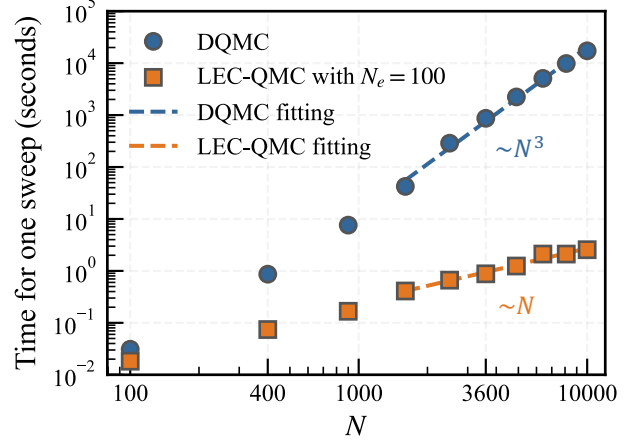


FIG. 1. Log-log plot of average CPU time per sweep vs. system size N . Parameters: $\Delta\tau = 0.1$, $U/t = 2.0$, $T/t = 1.0$, $N_e = 100$. The dashed lines show power-law fits, confirming the expected $O(N^3)$ scaling for DQMC (slope ≈ 3) and the superior $O(N)$ scaling for LEC-QMC (slope ≈ 1).

for all N spatial positions regardless of occupancy. To avoid this, we introduce an “on-the-fly” strategy that computes evolution data only for the specific particle being added, precisely when it is needed. This avoids computing the full $B_\mathbf{s}$ matrix. This approach, realized via a QR update algorithm [41], fundamentally reduces the computational complexity of the Fock state update.

For *particle addition* at site j , we append a column \mathbf{p} to P_η . Instead of forming the full propagator, we propagate only the new column \mathbf{p} through the time slices. To ensure stability, we perform orthogonalization against the existing stable basis Q_η (from the decomposition $B_\mathbf{s} P_\eta = Q_\eta R_\eta$) at each stabilization interval. At $\tau = \beta$, this yields an updated decomposition:

$$Q_{\eta'} = [Q_\eta | \mathbf{q}], \quad R_{\eta'} = \begin{pmatrix} R_\eta & \mathbf{r} \\ \mathbf{0} & r_{N_e+1} \end{pmatrix}. \quad (3)$$

The weight ratio simplifies to:

$$r = [\mathbf{p}^\dagger \mathbf{q} - \mathbf{p}^\dagger Q_\eta (P_\eta^\dagger Q_\eta)^{-1} P_\eta^\dagger \mathbf{q}] r_{N_e+1}. \quad (4)$$

Crucially, $(P_\eta^\dagger Q_\eta)^{-1}$ is already available from the Green’s function calculation. The cost is dominated by the propagation of one vector, scaling as $O(\beta N N_e)$. *Particle removal* is implemented via Givens rotations to restore the upper-triangular form of R after deleting a column, also scaling as $O(\beta N N_e)$.

Canonical sampling is achieved via particle-hole swap updates (one removal followed by one addition). A full sweep of N_e particles thus scales as $O(\beta N N_e^2)$. In the dilute limit where N_e is fixed and $N \rightarrow \infty$, the scaling is strictly linear in N .

Time scaling of the LEC-QMC method— To benchmark the performance of our LEC-QMC method, we ap-

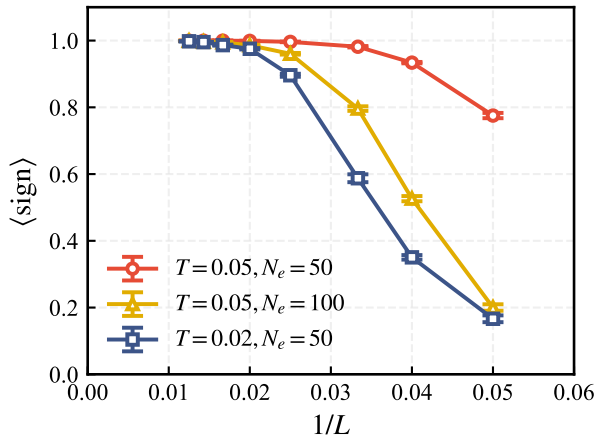


FIG. 2. Graph of the average sign $\langle \text{sign} \rangle$ versus system linear size L . When approaching the dilute limit $N = L^2 \gg N_e$, the system asymptotically has no sign problem.

ply it to the repulsive Hubbard model on a 2D square lattice

$$H = -t \sum_{\langle i,j \rangle, \sigma} (c_{i\sigma}^\dagger c_{j\sigma} + \text{h.c.}) + U \sum_i n_{i\uparrow} n_{i\downarrow} \quad (5)$$

First, we establish the computational complexity scaling. We compare the average CPU time per Monte Carlo sweep against standard DQMC (both using fast-update algorithm) for a system with $N_e = N_\uparrow + N_\downarrow = 100$, $U/t = 2.0$, and $T/t = 1.0$. The results are plotted versus system size N on a log-log scale (Fig. 1). As expected, standard DQMC shows a scaling of $O(N^3)$ (fit slope ≈ 3). In contrast, the LEC-QMC method exhibits a scaling of only $O(N)$ (fit slope ≈ 1). This demonstrates that LEC-QMC achieves an optimal linear scaling, fundamentally overcoming the cubic bottleneck of standard DQMC. This observed $O(N)$ scaling is in perfect agreement with the theoretical complexity of $O(\beta N N_e^2)$ derived in the above, as β and N_e are held constant in this benchmark. This scaling advantage translates into a dramatic, practical performance gain: for the largest systems benchmarked, a complete LEC-QMC sweep finishes within seconds under the given parameters. This represents an acceleration of over four orders of magnitude ($> 10^4 \times$) compared to the extrapolated time required by conventional DQMC, offering a decisive computational advantage for simulating large systems.

Sign problem in the dilute limit— The fermion sign problem is the primary obstacle in QMC. However, physical intuition suggests that in the dilute limit ($n \rightarrow 0$), fermions are spatially separated, suppressing the exchange processes responsible for negative signs. We verify this using LEC-QMC. Again, we consider the 2D square lattice Hubbard model. Fig. 2 shows the average sign as a function of linear system size L (where $N = L^2$) for a

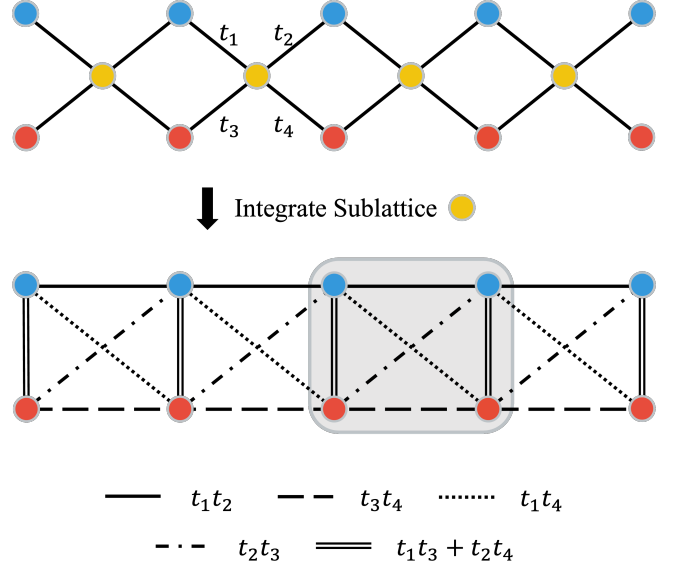


FIG. 3. Illustration of the effective flat-band model. The on-site energy of the effective Hamiltonian ($t_1^2 + t_2^2$ for sublattice A_1 and $t_3^2 + t_4^2$ for sublattice A_2) is omitted for clarity. The gray shaded region indicates the spatial extent of a localized Wannier function, which overlaps with its neighboring Wannier function on two sites.

fixed particle number N_e and fixed temperature. As the system size increases (density decreases), the average sign recovers from near zero to unity. This confirms that the dilute electron gas behaves increasingly like a Boltzmann gas, allowing LEC-QMC to simulate extremely large systems at low densities.

Flat-Band Ferromagnetism— Flat-band systems represent a singular limit where kinetic energy quenching amplifies interaction effects. To rigorously test our method, we construct a flat-band model using the bipartite crystalline lattice (BCL) framework in the chiral limit [43]. The original model has three sites in each unit cell, with two of them are the A sublattice, denotes as A_1 and A_2 , and the other one the B sublattice. By integrating out the B sublattice, we obtain an effective Hamiltonian featuring a perfectly flat lowest band and a gapped upper dispersive band. The illustration of the model is shown in Fig. 3. In our simulations, we choose the parameters $t_2 = t_3 = 1.0$, $t_1 = t_4 = -0.2$. By using Mielke-Tasaki's theorems on ferromagnetism in the Hubbard model [44], we can prove that the ground state of our 1D flat-band model at half-filling of the lowest flat band is ferromagnetic. However, numerical verification of this phase is notoriously difficult for standard grand-canonical QMC. The infinite compressibility associated with the singular density of states in a flat band makes the particle number extremely sensitive to the chemical potential, rendering precise doping control virtually impossible.

Our LEC-QMC method overcomes this filling-control

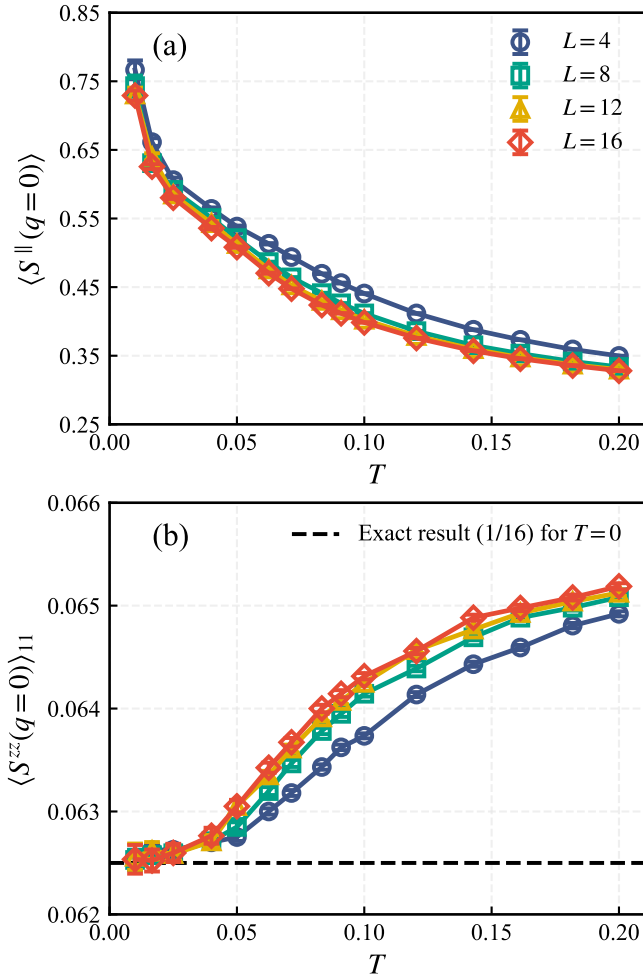


FIG. 4. Temperature evolution of (a) transverse and (b) longitudinal spin structure factors. The canonical ensemble constraint $\langle S_{\text{tot}}^z = 0 \rangle$ confines the magnetic moment to the XY-plane, enforcing the sum rule $\langle S_{zz}(q=0) \rangle_{11} = \langle S_{zz}(q=0) \rangle_{22} = -\langle S_{zz}(q=0) \rangle_{12} = -\langle S_{zz}(q=0) \rangle_{21}$.

problem by enforcing the particle number constraint explicitly. We simulate the 1D flat-band model strictly at half-filling. We simulate in the total S^z equals zero sector ($N_{\uparrow} = N_{\downarrow}$). To diagnose the magnetic order, we compute the equal-time uniform in-plane spin structure factor, defined as $S_{\parallel}(\mathbf{q} = 0) = \frac{1}{L} \sum_{i,j} \langle S_i^x S_j^x + S_i^y S_j^y \rangle$. While the Mermin-Wagner theorem precludes breaking of continuous symmetry at finite temperature in 1D, the ground state ferromagnetism manifests as a divergence of the correlation length as $T \rightarrow 0$. Our results show that $S_{\parallel}(\mathbf{q} = 0)$ increases in the low-temperature limit. In addition, we also calculate the out-of-plane spin structure factor of A_1 sublattice, and found it approaches a constant value 1/16 in the low temperature limit, consistent with the analytical result [45]. This provides unbiased numerical confirmation of the Mielke-Tasaki mechanism and demonstrates the capability of LEC-QMC to resolve ground-state properties in interacting systems with flat

bands.

Conclusion— We have developed LEC-QMC, an unbiased quantum Monte Carlo framework that enforces exact particle number conservation while achieving linear computational scaling $O(N)$ in the dilute limit. By combining a canonical-ensemble sampling strategy with a numerically stabilized QR update, we overcome the cubic-scaling bottleneck of conventional determinantal algorithms. We have demonstrated the power of this approach by explicitly mapping the restoration of sign coherence in the dilute electron gas and by confirming the ferromagnetic ground state of flat-band systems—a regime where standard grand-canonical methods fail due to singular compressibility.

The implications of this work extend beyond dilute systems. The LEC-QMC framework is structurally flexible and can be seamlessly integrated with constrained-path auxiliary-field methods [46, 47] to avoid the sign problem in dense, strongly correlated regimes, such as the doped Hubbard model near half-filling. We outlined the formalism on how to apply constrained path in LEC-QMC in SM [45]. By decoupling the ensemble constraint from the sign problem, our method would be suitable for probing phase diagrams in Wigner crystals, moiré superlattices, and ultracold atomic gases with unprecedented precision and scale.

Acknowledgments— We thank Zhida Song for helpful discussions. We acknowledge the support of the National Natural Science Foundation of China (Grants No. 12447103, No. 12274289, No. 12474245), the National Key R&D Program of China (Grant No. 2022YFA1402702, No. 2021YFA1401400), the Innovation Program for Quantum Science and Technology (under Grant No. 2021ZD0301902), Yangyang Development Fund, and Shanghai Jiao Tong University 2030 Initiative. The computations in this paper were run on the Siyuan-1 and π 2.0 clusters supported by the Center for High Performance Computing at Shanghai Jiao Tong University.

* chenkun@itp.ac.cn
 † xiaoyanxu@sjtu.edu.cn

[1] E. Wigner, On the Interaction of Electrons in Metals, *Phys. Rev.* **46**, 1002 (1934).

[2] D. M. Ceperley and B. J. Alder, Ground State of the Electron Gas by a Stochastic Method, *Phys. Rev. Lett.* **45**, 566 (1980).

[3] B. Tanatar and D. M. Ceperley, Ground state of the two-dimensional electron gas, *Phys. Rev. B* **39**, 5005 (1989).

[4] N. D. Drummond and R. J. Needs, Phase Diagram of the Low-Density Two-Dimensional Homogeneous Electron Gas, *Phys. Rev. Lett.* **102**, 126402 (2009).

[5] C. Attaccalite, S. Moroni, P. Gori-Giorgi, and G. B. Bachelet, Correlation Energy and Spin Polarization in the 2D Electron Gas, *Phys. Rev. Lett.* **88**, 256601 (2002).

[6] J. F. Schooley, W. R. Hosler, and M. L. Cohen, Superconductivity in Semiconducting SrTiO_3 , *Phys. Rev. Lett.* **12**, 474 (1964).

[7] X. Lin, G. Bridoux, A. Gourgout, G. Seyfarth, S. Krämer, M. Nardone, B. Fauqué, and K. Behnia, Critical Doping for the Onset of a Two-Band Superconducting Ground State in $\text{SrTiO}_3-\delta$, *Phys. Rev. Lett.* **112**, 207002 (2014).

[8] N. Reyren, S. Thiel, A. Caviglia, L. F. Kourkoutis, G. Hammerl, C. Richter, C. W. Schneider, T. Kopp, A.-S. Ruetschi, D. Jaccard, *et al.*, Superconducting interfaces between insulating oxides, *Science* **317**, 1196 (2007).

[9] E. Tang, J.-W. Mei, and X.-G. Wen, High-Temperature Fractional Quantum Hall States, *Phys. Rev. Lett.* **106**, 236802 (2011).

[10] T. Neupert, L. Santos, C. Chamon, and C. Mudry, Fractional Quantum Hall States at Zero Magnetic Field, *Phys. Rev. Lett.* **106**, 236804 (2011).

[11] K. Sun, Z. Gu, H. Katsura, and S. Das Sarma, Nearly Flatbands with Nontrivial Topology, *Phys. Rev. Lett.* **106**, 236803 (2011).

[12] F. D. M. Haldane, Geometrical Description of the Fractional Quantum Hall Effect, *Phys. Rev. Lett.* **107**, 116801 (2011).

[13] N. Regnault and B. A. Bernevig, Fractional Chern Insulator, *Phys. Rev. X* **1**, 021014 (2011).

[14] D. Sheng, Z.-C. Gu, K. Sun, and L. Sheng, Fractional quantum Hall effect in the absence of Landau levels, *Nature communications* **2**, 389 (2011).

[15] J. Dong, T. Wang, T. Wang, T. Soejima, M. P. Zaletel, A. Vishwanath, and D. E. Parker, Anomalous Hall Crystals in Rhombohedral Multilayer Graphene. I. Interaction-Driven Chern Bands and Fractional Quantum Hall States at Zero Magnetic Field, *Phys. Rev. Lett.* **133**, 206503 (2024).

[16] T. Soejima, J. Dong, T. Wang, T. Wang, M. P. Zaletel, A. Vishwanath, and D. E. Parker, Anomalous Hall crystals in rhombohedral multilayer graphene. II. General mechanism and a minimal model, *Phys. Rev. B* **110**, 205124 (2024).

[17] Z. Dong, A. S. Patri, and T. Senthil, Theory of quantum anomalous Hall phases in pentalayer rhombohedral graphene moiré structures, *Physical Review Letters* **133**, 206502 (2024).

[18] Z. Dong, A. Patri, and T. Senthil, Stability of anomalous Hall crystals in multilayer rhombohedral graphene (2024), arXiv preprint arXiv:2403.07873.

[19] A. S. Patri, Z. Dong, and T. Senthil, Extended quantum anomalous Hall effect in moiré structures: phase transitions and transport, arXiv preprint arXiv:2408.11818 (2024).

[20] R. Blankenbecler, D. J. Scalapino, and R. L. Sugar, Monte Carlo calculations of coupled boson-fermion systems. I, *Phys. Rev. D* **24**, 2278 (1981).

[21] N. Prokof'ev and B. Svistunov, Fermi-polaron problem: Diagrammatic Monte Carlo method for divergent sign-alternating series, *Phys. Rev. B* **77**, 020408 (2008).

[22] K. Chen and K. Haule, A combined variational and diagrammatic quantum Monte Carlo approach to the many-electron problem, *Nature communications* **10**, 3725 (2019).

[23] F. Assaad and H. Evertz, World-line and determinantal quantum Monte Carlo methods for spins, phonons and electrons, in *Computational Many-Particle Physics* (Springer, 2008) pp. 277–356.

[24] E. Y. Loh, J. E. Gubernatis, R. T. Scalettar, S. R. White, D. J. Scalapino, and R. L. Sugar, Sign problem in the numerical simulation of many-electron systems, *Phys. Rev. B* **41**, 9301 (1990).

[25] M. Troyer and U.-J. Wiese, Computational Complexity and Fundamental Limitations to Fermionic Quantum Monte Carlo Simulations, *Phys. Rev. Lett.* **94**, 170201 (2005).

[26] F. Sun and X. Y. Xu, Delay Update in Determinant Quantum Monte Carlo, *Physical Review B* **109**, 10.1103/physrevb.109.235140 (2024).

[27] F. Sun and X. Y. Xu, Boosting Determinant Quantum Monte Carlo with Submatrix Updates: Unveiling the Phase Diagram of the 3D Hubbard Model, *SciPost Physics* **18**, 10.21468/scipostphys.18.2.055 (2025).

[28] J. Liu, Y. Qi, Z. Y. Meng, and L. Fu, Self-Learning Monte Carlo Method, *Physical Review B* **95**, 041101 (2017).

[29] X. Y. Xu, Y. Qi, J. Liu, L. Fu, and Z. Y. Meng, Self-Learning Quantum Monte Carlo Method in Interacting Fermion Systems, *Physical Review B* **96**, 041119 (2017).

[30] G. Pan, C. Chen, and Z. Y. Meng, *Self-Learning Monte Carlo Method: A Review* (2025).

[31] Y.-Y. He, H. Shi, and S. Zhang, Reaching the Continuum Limit in Finite-Temperature *Ab Initio* Field-Theory Computations in Many-Fermion Systems, *Physical Review Letters* **123**, 136402 (2019).

[32] C. Gilbreth, S. Jensen, and Y. Alhassid, Reducing the complexity of finite-temperature auxiliary-field quantum Monte Carlo, *Computer Physics Communications* **264**, 107952 (2021).

[33] G. H. Lang, C. W. Johnson, S. E. Koonin, and W. E. Ormand, Monte Carlo evaluation of path integrals for the nuclear shell model, *Phys. Rev. C* **48**, 1518 (1993).

[34] W. E. Ormand, D. J. Dean, C. W. Johnson, G. H. Lang, and S. E. Koonin, Demonstration of the auxiliary-field Monte Carlo approach for sd-shell nuclei, *Phys. Rev. C* **49**, 1422 (1994).

[35] C. N. Gilbreth and Y. Alhassid, Pair condensation in a finite trapped Fermi gas, *Phys. Rev. A* **88**, 063643 (2013).

[36] Z. Wang, F. F. Assaad, and F. Parisen Toldin, Finite-size effects in canonical and grand-canonical quantum Monte Carlo simulations for fermions, *Phys. Rev. E* **96**, 042131 (2017).

[37] Y. Ouyang and X. Y. Xu, Projection of infinite- U Hubbard model and algebraic sign structure, *Phys. Rev. B*

104, L241104 (2021).

[38] T. Shen, H. Barghathi, J. Yu, A. Del Maestro, and B. M. Rubenstein, Stable recursive auxiliary field quantum Monte Carlo algorithm in the canonical ensemble: Applications to thermometry and the Hubbard model, *Phys. Rev. E* **107**, 055302 (2023).

[39] S. Humeniuk and Y. Wan, Numerically Exact Mimicking of Quantum Gas Microscopy for Interacting Lattice Fermions, *Physical Review B* **104**, 075155 (2021).

[40] S. Ding, S. Li, and Y. Wang, Sampling Electronic Fock States Using Determinant Quantum Monte Carlo, *Communications Physics* **8**, 10.1038/s42005-025-01963-z (2025).

[41] G. H. Golub and C. F. Van Loan, *Matrix Computations*, fourth edition ed., Johns Hopkins Studies in the Mathematical Sciences (The Johns Hopkins University Press, Baltimore, 2013).

[42] H. Du and Y.-Y. He, Accelerating ground-state auxiliary-field quantum Monte Carlo simulations by delayed update and block force-bias update, *Phys. Rev. B* **112**, 235120 (2025).

[43] D. Călugăru, A. Chew, L. Elcoro, Y. Xu, N. Regnault, Z.-D. Song, and B. A. Bernevig, General construction and topological classification of crystalline flat bands, *Nature Physics* **18**, 185 (2022).

[44] A. Mielke and H. Tasaki, Ferromagnetism in the Hubbard model: Examples from models with degenerate single-electron ground states, *Communications in mathematical physics* **158**, 341 (1993).

[45] See Supplemental Material(SM) for more details..

[46] S. Zhang, J. Carlson, and J. E. Gubernatis, A Constrained Path Monte Carlo Method for Fermion Ground States, *Physical Review B* **55**, 7464 (1997).

[47] Y.-Y. He, M. Qin, H. Shi, Z.-Y. Lu, and S. Zhang, Finite-temperature auxiliary-field quantum Monte Carlo: Self-consistent constraint and systematic approach to low temperatures, *Physical Review B* **99**, 045108 (2019).

Supplementary material for “Linear Canonical-Ensemble Quantum Monte Carlo: From Dilute Fermi Gas to Flat-Band Ferromagnetism”

I. DETAILS OF LEC-QMC

In this section, we detail the implementation of the LEC-QMC algorithm, focusing specifically on the efficient update procedures for the Fock state. The core problem we want to solve is obtaining the new QR decomposition $Q_{\eta'} R_{\eta'} = B_s P_{\eta'}$ efficiently when a particle is added or removed. The main algorithm based on is the QR update algorithm [S1].

A. Adding a particle

Consider the scenario where a new particle is added to the system. This operation mathematically corresponds to appending a new column vector \mathbf{p} to the existing Fock state matrix P_{η} :

$$P_{\eta'} = [P_{\eta} \mid \mathbf{p}] \quad (\text{S1})$$

A straightforward approach to update the decomposition is to propagate the new particle vector $\mathbf{w} = B_s(\beta, 0)\mathbf{p}$ and subsequently perform a modified Gram-Schmidt (MGS) orthogonalization against the existing basis Q_{η} . This would yield the new basis vector \mathbf{q} and the updated components:

$$\mathbf{v} = Q_{\eta}^{\dagger} \mathbf{w} \quad (\text{S2})$$

$$\mathbf{q} = \frac{\mathbf{w} - Q_{\eta} \mathbf{v}}{\|\mathbf{w} - Q_{\eta} \mathbf{v}\|} \quad (\text{S3})$$

$$r_{N_e+1} = \|\mathbf{w} - Q_{\eta} \mathbf{v}\| \quad (\text{S4})$$

The resulting QR decomposition for the updated state $P_{\eta'}$ would be:

$$B_s(\beta, 0)P_{\eta'} = Q_{\eta'} R_{\eta'} \quad (\text{S5})$$

$$Q_{\eta'} = [Q_{\eta} \mid \mathbf{q}], \quad R_{\eta'} = \begin{bmatrix} R_{\eta} & \mathbf{v} \\ \mathbf{0} & r_{N_e+1} \end{bmatrix} \quad (\text{S6})$$

Based on this structure, the weight ratio for the particle addition can be derived as:

$$\begin{aligned} r &= \frac{\det[P_{\eta'}^{\dagger} B_s(\beta, 0) P_{\eta'}]}{\det[P_{\eta}^{\dagger} B_s(\beta, 0) P_{\eta}]} \\ &= \frac{\det[P_{\eta'}^{\dagger} Q_{\eta'}] \det[R_{\eta'}]}{\det[P_{\eta}^{\dagger} Q_{\eta}]} \frac{\det[R_{\eta'}]}{\det[R_{\eta}]} \\ &= [\mathbf{p}^{\dagger} \mathbf{q} - \mathbf{p}^{\dagger} Q_{\eta} (P_{\eta}^{\dagger} Q_{\eta})^{-1} P_{\eta}^{\dagger} \mathbf{q}] r_{N_e+1} \\ &= s r_{N_e+1} \end{aligned} \quad (\text{S7})$$

where s denotes the Schur complement in the brackets, and the matrix $(P_{\eta}^{\dagger} Q_{\eta})^{-1}$ is a standard byproduct of the Green's function calculation in PQMC.

While the direct approach above is theoretically sound, the propagator $B_s(\beta, 0)$ becomes singular at low temperatures, rendering the direct MGS numerically unstable. To overcome this, we perform a layer-by-layer QR update at each stabilization step (we perform numerical stabilization every τ_w time slices, and in total we perform $n = L_{\tau}/\tau_w$ stabilization steps), analogous to the standard PQMC sweep. The schematic of this process is illustrated in Fig. S1(a), and the detailed procedure is as follows:

1. First Stabilization Step ($i = 1$):

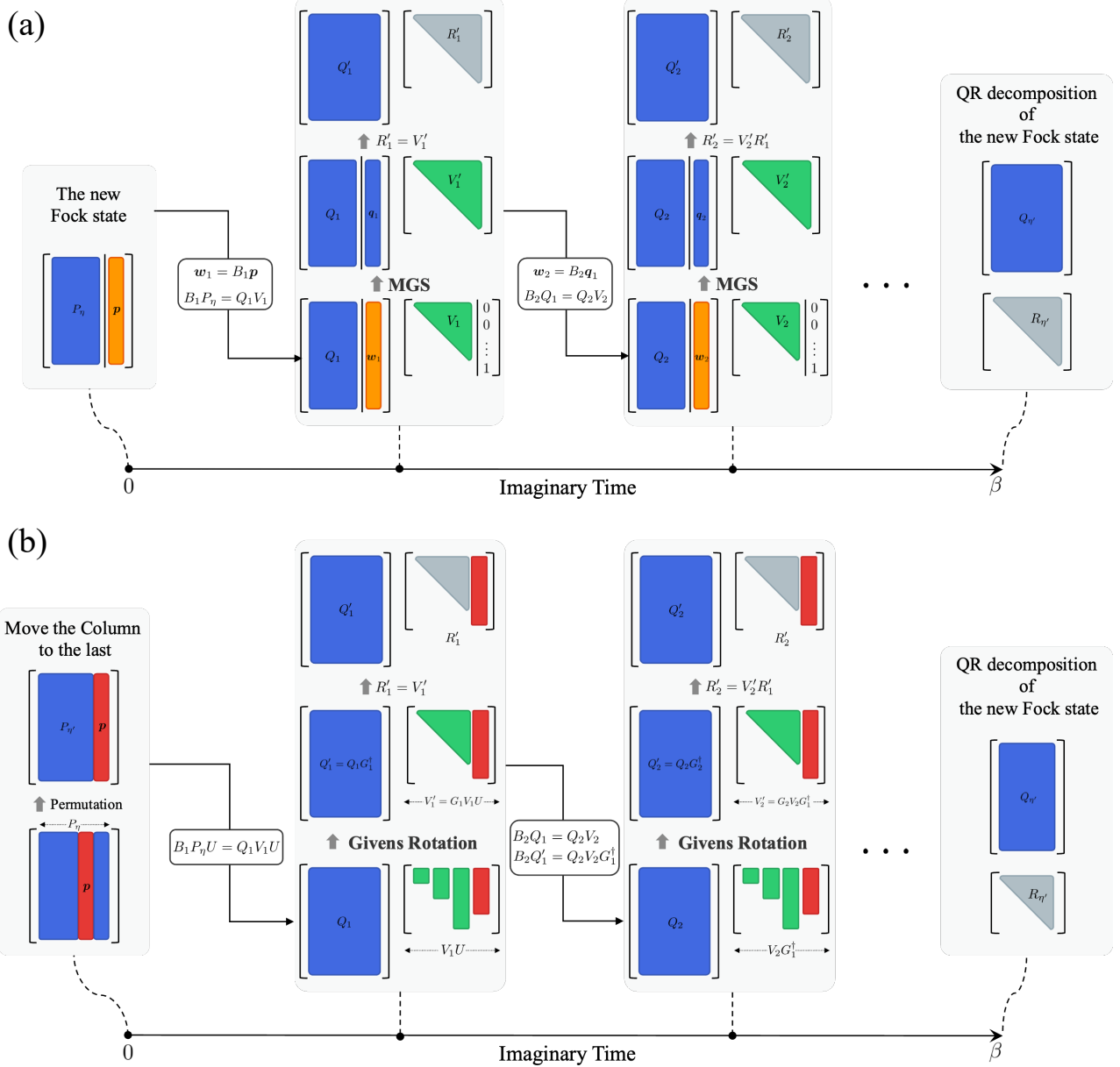


FIG. S1. The two fundamental update processes in the LEC-QMC method. (a) Adding a new particle (the orange column) to the system. We perform propagation on the new column. At every numerical stabilization step, we perform the modified Gram-Schmidt orthogonalization to get the QR decomposition of the new Fock state. (b) Removing a particle (the red column) from the system. We first apply a permutation to move the column to the last position, then apply Givens rotations at every numerical stabilization step to restore the triangular structure of the matrix. The QR decomposition of the new Fock state is obtained by truncating the last column and row of the matrices.

- **Propagate and Orthogonalize:** Apply the propagator $B_1 \equiv B_s(\tau_w, 0)$ to the new particle \mathbf{p} and orthogonalize the result against the basis Q_1 :

$$\begin{aligned} \mathbf{w}_1 &= B_1 \mathbf{p} \\ \mathbf{v}_1 &= Q_1^\dagger \mathbf{w}_1 \\ \mathbf{q}_1 &= \frac{\mathbf{w}_1 - Q_1 \mathbf{v}_1}{\|\mathbf{w}_1 - Q_1 \mathbf{v}_1\|} \end{aligned}$$

- **Update Matrices:** Construct the augmented basis Q'_1 and the “transfer matrix” V'_1 . Note that R'_1 is

initialized simply as V'_1 :

$$Q'_1 = \left[Q_1 \middle| \mathbf{q}_1 \right], \quad R'_1 = V'_1 = \begin{bmatrix} V_1 & \mathbf{v}_1 \\ \mathbf{0} & \|\mathbf{w}_1 - Q_1 \mathbf{v}_1\| \end{bmatrix}$$

2. Subsequent Stabilization Steps ($i > 1$):

Recall that for the original N_e particles, the QR propagation $B_i Q_{i-1} = Q_i V_i$ has already been computed and stored. Here, $B_i \equiv B_s(i\tau_w, 0)$ and V_i serves as the “transfer matrix” for the existing basis. We leverage these pre-computed matrices to perform an efficient update:

- **Propagate and Orthogonalize:** Propagate the new basis vector \mathbf{q}_{i-1} from the previous step and orthogonalize it against the current basis Q_i :

$$\begin{aligned} \mathbf{w}_i &= B_i \mathbf{q}_{i-1} \\ \mathbf{v}_i &= Q_i^\dagger \mathbf{w}_i \quad (\text{Projection onto existing basis}) \\ \mathbf{q}_i &= \frac{\mathbf{w}_i - Q_i \mathbf{v}_i}{\|\mathbf{w}_i - Q_i \mathbf{v}_i\|} \quad (\text{Normalization of residual}) \end{aligned}$$

- **Augment Basis and Transfer Matrix:** Construct the updated basis Q'_i and the “transfer matrix” V'_i by appending the new components. The block structure preserves the existing dynamics in the upper-left block:

$$Q'_i = [Q_i \mid \mathbf{q}_i], \quad V'_i = \begin{bmatrix} V_i & \mathbf{v}_i \\ \mathbf{0} & \|\mathbf{w}_i - Q_i \mathbf{v}_i\| \end{bmatrix}$$

- **Update Accumulated R Matrix:** Update the triangular matrix via the recurrence relation $R'_i = V'_i R'_{i-1}$. Crucially, since the first N_e columns of both V'_i and R'_{i-1} are identical to the pre-computed values, we only need to compute the last column of R'_i :

$$[R'_i]_{:, N_e+1} = V'_i [R'_{i-1}]_{:, N_e+1}$$

This reduces the complexity of this step to $O(NN_e)$.

3. Final Stabilization Step and Update:

- At the final stabilization step, we obtain the full QR decomposition of the updated Fock state $P_{\eta'}$, with $Q_{\eta'} = Q'_n$ and $R_{\eta'} = R'_n$.
- We calculate the weight ratio using Eq. (S7).
- **If the update is accepted**, we must update the inverse matrix $(P_\eta^\dagger Q_\eta)^{-1}$ to accelerate the next sweep. This is done efficiently using the blockwise inversion formula:

$$(P_{\eta'}^\dagger Q_{\eta'})^{-1} = \begin{bmatrix} (P_\eta^\dagger Q_\eta)^{-1} + \frac{1}{s} (P_\eta^\dagger Q_\eta)^{-1} P_\eta^\dagger \mathbf{q} \mathbf{p}^\dagger Q_\eta (P_\eta^\dagger Q_\eta)^{-1} & -\frac{1}{s} (P_\eta^\dagger Q_\eta)^{-1} P_\eta^\dagger \mathbf{q} \\ -\frac{1}{s} \mathbf{p}^\dagger Q_\eta (P_\eta^\dagger Q_\eta)^{-1} & \frac{1}{s} \end{bmatrix} \quad (\text{S8})$$

Complexity Analysis: The computational cost of a single QR update step is $O(NN_e)$. Since the number of numerical stabilization steps (n) scales linearly with the inverse temperature, $n \propto \beta$, the total complexity for adding a particle is $O(\beta NN_e)$.

B. Removing a particle

Removing a particle from the system is structurally more complex than adding one because it disrupts the column ordering. The simplest case is removing the last particle (the last column of P_η), which merely requires deleting the last columns of Q and R .

To remove the k -th particle, we employ a strategy of permutation followed by retriangulation. We first apply a permutation matrix U to move the k -th column of P_η to the last position. Since the permutation does not change the weight of the Fock state:

$$\det [P_\eta^\dagger B(\beta, 0) P_\eta] = \det [U^\dagger P_\eta^\dagger B(\beta, 0) P_\eta U] \quad (\text{S9})$$

we can proceed by updating the QR decomposition of the permuted system. The process involves applying Givens rotations to restore the upper-triangular structure of the R (or V) matrices. The schematic is shown in Fig. S1(b).

1. First Stabilization Step ($i = 1$):

- **Permute and Retriangulate:** Apply the permutation U to V_1 and then a Givens rotation G_1 to restore the triangular structure. The updated “transfer matrix” V'_1 is:

$$V'_1 = G_1 V_1 U$$

- **Update Basis:** The basis is updated to absorb the unitary transformation:

$$Q'_1 = Q_1 G_1^\dagger$$

- **Update R Matrix:** For the first stabilization step, the total R matrix is simply:

$$R'_1 = V'_1$$

We can verify: $B_1(P_\eta U) = Q_1(G_1^\dagger G_1) V_1 U = Q'_1 V'_1$.

2. Subsequent Stabilization Steps ($i > 1$):

- **Propagate Permutation:** The propagator relationship becomes $B_i Q'_{i-1} = Q_i (V_i G_{i-1}^\dagger)$. We need a new Givens rotation G_i to make the term in parentheses upper-triangular.

- **Retriangulate:**

$$V'_i = G_i (V_i G_{i-1}^\dagger)$$

- **Update Basis and R Matrix:**

$$\begin{aligned} Q'_i &= Q_i G_i^\dagger \\ R'_i &= V'_i R'_{i-1} = G_i R_i U \end{aligned}$$

3. Final Stabilization Step and Inverse Update:

- **Truncation:** After the final stabilization step, the particle to be removed is at the last position. The new QR factors $Q_{\eta'}$ and $R_{\eta'}$ are obtained by simply removing the last column of Q'_n and the last row/column of R'_n .

- **Weight Ratio:** The ratio is derived as:

$$\begin{aligned} r &= \frac{\det[R_{\eta'}]}{\det[R_\eta]} \frac{\det[P_{\eta'}^\dagger Q_{\eta'}]}{\det[P_\eta^\dagger Q_\eta]} \\ &= \frac{1}{s r_{N_e}} \end{aligned} \quad (\text{S10})$$

where r_{N_e} is the last diagonal element of the permuted R matrix.

- **Updating the Inverse Matrix:** If the update is accepted, we need to calculate the inverse matrix for the new system $(P_{\eta'}^\dagger Q_{\eta'})^{-1}$. First, we compute the inverse of the full permuted matrix, let us denote it as \mathcal{M}^{-1} :

$$\mathcal{M}^{-1} = [(P_\eta U)^\dagger Q'_n]^{-1} = G_n (P_\eta^\dagger Q_\eta)^{-1} U$$

Considering the block structure of this matrix \mathcal{M}^{-1} , we have the following identity relating it to the target inverse $(P_{\eta'}^\dagger Q_{\eta'})^{-1}$:

$$\mathcal{M}^{-1} = \begin{bmatrix} (P_{\eta'}^\dagger Q_{\eta'})^{-1} + \frac{1}{s} \mathbf{u} \mathbf{v}^\dagger & -\frac{1}{s} \mathbf{u} \\ -\frac{1}{s} \mathbf{v}^\dagger & \frac{1}{s} \end{bmatrix} \quad (\text{S11})$$

where \mathbf{u} and \mathbf{v} are vectors derived from the column updates. The scalar $1/s$ is simply the bottom-right element of \mathcal{M}^{-1} . Therefore, the inverse matrix for the reduced system can be extracted directly from the sub-blocks of \mathcal{M}^{-1} :

$$(P_{\eta'}^\dagger Q_{\eta'})^{-1} = [\mathcal{M}^{-1}]_{1:(N_e-1), 1:(N_e-1)} - \frac{[\mathcal{M}^{-1}]_{1:(N_e-1), N_e} \times [\mathcal{M}^{-1}]_{N_e, 1:(N_e-1)}}{[\mathcal{M}^{-1}]_{N_e, N_e}} \quad (\text{S12})$$

The computational cost of a single QR update step for removing a particle is dominated by the Givens rotations with complexity $O(NN_e)$. Again, since the number of numerical stabilization steps (n) scales linearly with the inverse temperature, $n \propto \beta$, the total complexity for removing a particle is also $O(\beta NN_e)$.

II. BENCHMARK OF THE LEC-QMC METHOD

To ensure the accuracy of LEC-QMC, we perform a benchmark for the 2D repulsive Hubbard model. We choose the system with size $L = 4$ and particle number $N_e = N_\uparrow + N_\downarrow = 2$, which can be benchmarked by the exact diagonalization (ED) method. We calculated the spin correlation function $\langle \hat{\mathbf{S}}(\mathbf{r}_i) \hat{\mathbf{S}}(\mathbf{r}_j) \rangle$ and the charge density correlation function $\langle \hat{n}(\mathbf{r}_i) \hat{n}(\mathbf{r}_j) \rangle$. The results are shown in Fig. S2, which agree well with ED.

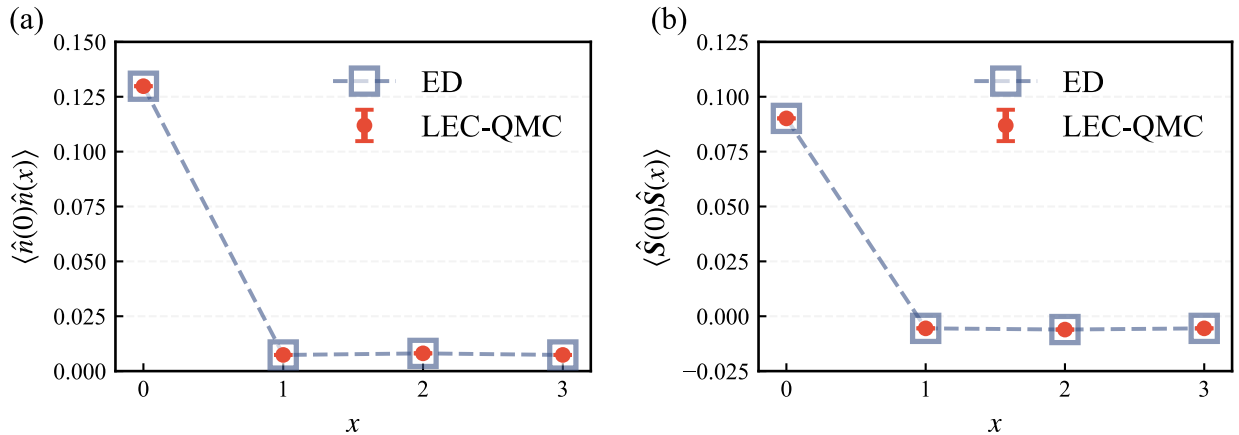


FIG. S2. Benchmark LEC-QMC results with ED. The parameters used in the simulations are $\Delta\tau = 0.05$, $L = 4$, $N_e = 2$, $T = 0.05$ and $U = 2.0$.

III. CONSTRUCTION OF THE FLAT BAND MODEL

In this section, we detail the construction of the flat-band model via the bipartite crystalline lattice (BCL) formalism and its chiral limit reduction proposed in Ref. [S2].

A. Analysis of the general BCL Hamiltonian

We consider a system with three bands, defined on a bipartite lattice structure. The basis is chosen such that the first two components correspond to the majority sublattice (site A_1 and site A_2), and the third component corresponds to the minority sublattice (site B). The Hamiltonian in momentum space is given by:

$$H(\vec{k}) = \begin{pmatrix} a & 0 & S_1(\vec{k}) \\ 0 & a & S_2(\vec{k}) \\ S_1^*(\vec{k}) & S_2^*(\vec{k}) & B(\vec{k}) \end{pmatrix} \quad (\text{S13})$$

where a and $B(\vec{k})$ represent the onsite potentials (or intra-sublattice terms) for the two sublattices, and $S_{1,2}(\vec{k})$ describe the hopping between the sublattices.

By solving the characteristic equation, we obtain the three eigenvalues:

$$\lambda_1 = a, \quad (\text{S14})$$

$$\lambda_{2,3} = \frac{1}{2} \left[a + B(\vec{k}) \mp \sqrt{(a - B(\vec{k})^2 + 4(|S_1(\vec{k})|^2 + |S_2(\vec{k})|^2)} \right]. \quad (\text{S15})$$

The band $\lambda_1 = a$ is perfectly flat. For our purposes, we require this flat band to be the strictly lowest energy band. However, the general BCL construction described above cannot directly satisfy this condition with non-zero diagonal terms. As extensively discussed in Ref. [S2], to realize the flat band as the lowest band, one needs to consider a specific limit or “integrate out” certain degrees of freedom to obtain an effective low-energy model.

B. The chiral limit and effective Hamiltonian

To realize the flat band as the ground state, we consider the chiral limit by setting $a = 0$ and $B(\vec{k}) = 0$. The Hamiltonian simplifies to a purely off-diagonal block form:

$$H_{\text{chiral}}(\vec{k}) = \begin{pmatrix} 0 & 0 & S_1(\vec{k}) \\ 0 & 0 & S_2(\vec{k}) \\ S_1^*(\vec{k}) & S_2^*(\vec{k}) & 0 \end{pmatrix} = \begin{pmatrix} \mathbf{0}_{2 \times 2} & \mathbf{S}(\vec{k}) \\ \mathbf{S}^\dagger(\vec{k}) & 0 \end{pmatrix}, \quad (\text{S16})$$

where $\mathbf{S}(\vec{k}) = [S_1(\vec{k}), S_2(\vec{k})]^T$ is a column vector.

To obtain the low-energy effective physics, we “integrate out” the minority sublattice (the third row/column). Mathematically, this is equivalent to considering the squared Hamiltonian H^2 or the projection onto the majority sublattice. The effective Hamiltonian for the two sites in the majority sublattice corresponds to the 2×2 block $\mathbf{S}(\vec{k})\mathbf{S}^\dagger(\vec{k})$:

$$H_{\text{eff}}(\vec{k}) = \mathbf{S}(\vec{k})\mathbf{S}^\dagger(\vec{k}) = \begin{pmatrix} |S_1(\vec{k})|^2 & S_1(\vec{k})S_2^*(\vec{k}) \\ S_2(\vec{k})S_1^*(\vec{k}) & |S_2(\vec{k})|^2 \end{pmatrix}. \quad (\text{S17})$$

The eigenvalues of this effective Hamiltonian are straightforwardly:

$$\lambda_1 = 0, \quad \lambda_2 = |S_1(\vec{k})|^2 + |S_2(\vec{k})|^2. \quad (\text{S18})$$

Here, $\lambda_1 = 0$ corresponds to the perfectly flat ground state, and λ_2 forms the dispersive excited band. This effective model H_{eff} successfully isolates the flat band at zero energy.

We implement this scheme in a one-dimensional lattice model using the coupling functions:

$$S_1(k) = t_1 + t_2 e^{-ik}, \quad S_2(k) = t_3 + t_4 e^{-ik}, \quad (\text{S19})$$

where t_1, t_2, t_3 and t_4 are all set as real hopping for simplicity. In our simulations, we set $t_1 = t_4 = -0.2$ and $t_2 = t_3 = 1.0$, and the graph of model in real space is shown in Fig. 3 of the main text.

IV. PROOF OF FERROMAGNETIC GROUND STATE

In this section, we provide a rigorous proof that the ground state of the model illustrated in Fig. 3 of the main text is ferromagnetic. Following the theoretical framework established in Ref. [S3, S4], our derivation proceeds in two steps: we first construct the localized Wannier functions, and then apply the completeness and connectivity conditions to demonstrate the uniqueness of the ferromagnetic ground state.

A. Exact construction of compact localized states

To derive the explicit form of the Wannier functions in real space, we first solve for the zero-energy eigenstate in momentum space. The condition for a zero mode, $H_{\text{eff}}|\psi_k\rangle = 0$, implies $\mathbf{S}^\dagger(\vec{k})|\psi_k\rangle = 0$. Therefore, the components of $|\psi_k\rangle$ in plane wave basis ($|A_{1,k}\rangle$, $|A_{2,k}\rangle$) can have the following form up to a normalization factor,

$$\psi_{A_1}(k) = S_2^*(k), \quad \psi_{A_2}(k) = -S_1^*(k) \quad (\text{S20})$$

To obtain the real-space Wannier function $|W_R\rangle$ centered at unit cell R , we perform the inverse Fourier transform:

$$|W_R\rangle = \frac{1}{\sqrt{N}} \sum_k e^{-ikR} |\psi_k\rangle \quad (\text{S21})$$

Substituting Eq. (S20) into Eq. (S21) and utilizing the relation between site basis and plane wave basis,

$$\frac{1}{N} \sum_k e^{-ikR} |A_{1,k}\rangle = |A_{1,R}\rangle, \quad (\text{S22})$$

$$\frac{1}{N} \sum_k e^{-ikR} |A_{2,k}\rangle = |A_{2,R}\rangle, \quad (\text{S23})$$

we derive the site-resolved amplitudes. We get

$$|W_R\rangle = t_3 |A_{1,R}\rangle + t_4 |A_{1,R-1}\rangle - t_1 |A_{2,R}\rangle - t_2 |A_{2,R-1}\rangle \quad (\text{S24})$$

Thus, the effective flat band Wannier function is a compact localized state confined strictly to two adjacent unit cells in the effective lattice, as depicted by the shaded region in Fig. 3. It is straightforward to verify that for this localized state, the total hopping amplitude to any outside site vanishes.

B. Proof of ferromagnetism via Mielke-Tasaki mechanism

We now address the magnetic ground state of the system when the flat band is half-filled (filling factor $\nu = 1$, corresponding to $N_e = L$ electrons in a system of L unit cells) in the presence of a repulsive Hubbard interaction $U > 0$.

The stability of ferromagnetism in flat-band systems is governed by the connectivity of the local basis states, as established by Mielke and Tasaki. The proof relies on two conditions satisfied by our constructed basis $\{|W_R\rangle\}$:

1. **Completeness:** The set of Wannier functions $\{|W_R\rangle\}$ is linearly independent and spans the entire flat band manifold.
2. **Connectivity:** A crucial requirement for ferromagnetism is that the Wannier functions must overlap in real space to mediate exchange interactions.
 - Consider the Wannier function $|W_R\rangle$, which has support on cells $\{R, R-1\}$.
 - The adjacent function $|W_{R+1}\rangle$ has support on cells $\{R+1, R\}$.
 - Since both functions share support on the sites of unit cell R (specifically sites $A_{1,R}$ and $A_{2,R}$), their overlap integral is :

$$\langle W_R | W_{R+1} \rangle = t_1 t_2 + t_3 t_4 \quad (\text{S25})$$

As long as we choose parameters $t_1 t_2 + t_3 t_4 \neq 0$, their overlap is non-vanishing.

This non-vanishing overlap implies that the ground state manifold is connected. According to Mielke and Tasaki's theorems [S3] on positive semi-definite Hamiltonians, when the single-particle ground states are degenerate and satisfy this connectivity condition, the many-body ground state at half-filling is the unique ferromagnetic state with maximal total spin $S_{\text{tot}} = N_e/2$, apart from the trivial $(2S_{\text{tot}} + 1)$ -fold spin rotation degeneracy.

Any state with lower total spin would require constructing spatial domain walls or occupying higher energy bands to satisfy the Pauli exclusion principle, thereby incurring an energy penalty. Therefore, the system exhibits robust ferromagnetism driven by the geometric frustration and quantum interference inherent in the flat band.

Due to the SU(2) spin-rotation symmetry of the Hamiltonian, the ferromagnetic ground state possesses a $(2S_{\text{tot}}+1)$ -fold degeneracy. However, in our canonical ensemble simulations, we restrict the particle numbers such that $N_{\uparrow} = N_{\downarrow} = N_e/2$. This constraint selects the $S_{\text{tot}}^z = 0$ sector, effectively singling out a specific state within the ferromagnetic multiplet. Consequently, the observed ferromagnetic order manifests within the XY-plane, as shown in the main text.

V. EXACT CALCULATION OF SUBLATTICE SPIN FLUCTUATIONS

In this section, we provide a rigorous derivation of the squared sublattice magnetization $\langle (S_A^z)^2 \rangle$ for the ferromagnetic ground state in the spin sector $S_{\text{tot}}^z = 0$. This analytic result rationalizes the convergence value observed in Fig. 4(a).

A. Formalism

We consider a system of N_e electrons filling a completely flat band. The many-body ground state $|\Psi_0\rangle$ exhibits perfect ferromagnetism. In the sector with zero total z -component spin $S_{\text{tot}}^z = 0$, the wavefunction factorizes into a spin part and a spatial part: the spin component corresponds to the Dicke state $|S = N_e/2, M = 0\rangle$, while the spatial component is a Slater determinant formed by occupying all Bloch states $|\psi_k\rangle$ in the flat band.

The total spin- z operator on sublattice A is defined as:

$$S_A^z = \sum_{i=1}^{N_e} \hat{s}_i^z \hat{\mathcal{P}}_A(i), \quad (\text{S26})$$

where \hat{s}_i^z is the spin operator for the i -th electron, and $\hat{\mathcal{P}}_A(i)$ is the projection operator onto sublattice A for the i -th electron.

We aim to calculate the fluctuation $\langle (S_A^z)^2 \rangle = \langle \Psi_0 | (S_A^z)^2 | \Psi_0 \rangle$. Expanding the square yields single-particle and two-particle terms:

$$\begin{aligned} (S_A^z)^2 &= \sum_{i,j} \hat{s}_i^z \hat{s}_j^z \hat{\mathcal{P}}_A(i) \hat{\mathcal{P}}_A(j) \\ &= \sum_i (\hat{s}_i^z)^2 \hat{\mathcal{P}}_A(i) + \sum_{i \neq j} \hat{s}_i^z \hat{s}_j^z \hat{\mathcal{P}}_A(i) \hat{\mathcal{P}}_A(j). \end{aligned} \quad (\text{S27})$$

Due to the decoupled nature of spin and spatial degrees of freedom in the flat band ferromagnet, we can evaluate the expectation values of the spin and orbital operators separately.

B. Spin correlations

For the Dicke state $|S = N_e/2, M = 0\rangle$, the onsite spin fluctuation is $\langle (\hat{s}_i^z)^2 \rangle = \frac{1}{4}$. The total spin fluctuation vanishes, $\langle (\hat{S}_{\text{tot}}^z)^2 \rangle = \sum_{i,j} \langle \hat{s}_i^z \hat{s}_j^z \rangle = 0$, which implies a sum rule for the pair correlations:

$$\sum_{i \neq j} \langle \hat{s}_i^z \hat{s}_j^z \rangle = - \sum_i \langle (\hat{s}_i^z)^2 \rangle = - \frac{N_e}{4}. \quad (\text{S28})$$

By symmetry among identical fermions, the correlation between any distinct pair $i \neq j$ is uniform:

$$\langle \hat{s}_i^z \hat{s}_j^z \rangle = - \frac{1}{4(N_e - 1)}. \quad (\text{S29})$$

C. Spatial correlations in momentum space

The calculation of spatial projections is most conveniently performed in reciprocal space, where the Bloch basis is orthogonal. Let $p(k)$ denote the probability weight of the flat band eigenstate on sublattice A at momentum k :

$$p(k) = \langle \psi_k | \hat{\mathcal{P}}_A | \psi_k \rangle = \frac{|S_1(k)|^2}{|S_1(k)|^2 + |S_2(k)|^2}, \quad (\text{S30})$$

where $S_1(k)$ and $S_2(k)$ are the structure factors defined previously.

We define the moments of the sublattice weight as $P_n = \sum_k [p(k)]^n$. The expectation value of the single-particle projector is simply:

$$\sum_i \langle \hat{\mathcal{P}}_A(i) \rangle = \sum_k p(k) = P_1. \quad (\text{S31})$$

For the two-particle term, since the spatial wavefunction is a single Slater determinant of orthogonal Bloch states, the joint probability factorizes for distinct momenta:

$$\begin{aligned} \sum_{i \neq j} \langle \hat{\mathcal{P}}_A(i) \hat{\mathcal{P}}_A(j) \rangle &= \sum_{k \neq q} p(k)p(q) \\ &= \left(\sum_k p(k) \right)^2 - \sum_k [p(k)]^2 \\ &= P_1^2 - P_2. \end{aligned} \quad (\text{S32})$$

The term P_2 captures the momentum-space texture of the wavefunction arising from the interference between the hopping amplitudes.

D. Result

Substituting the spin and spatial components back into the expansion, we obtain the general formula:

$$\begin{aligned} \langle (S_A^z)^2 \rangle &= \frac{1}{4}P_1 + \left(-\frac{1}{4(N_e - 1)} \right) (P_1^2 - P_2) \\ &= \frac{1}{4(N_e - 1)} [(N_e - 1)P_1 - P_1^2 + P_2]. \end{aligned} \quad (\text{S33})$$

For the specific parameters used in our simulations ($t_1 = t_4 = t'$ and $t_2 = t_3 = t$), the Hamiltonian possesses a symmetry that enforces equal sublattice weights, $p(k) = 1/2$, independent of k . Consequently, the moments become $P_1 = N_e/2$ and $P_2 = N_e/4$. Substituting these into the general formula yields:

$$\langle (S_A^z)^2 \rangle = \frac{N_e}{16}, \quad (\text{S34})$$

$$\langle S^z(q=0) \rangle_{11} \equiv \frac{1}{L} \langle (S_A^z)^2 \rangle = \frac{1}{16}, \quad (\text{S35})$$

where we have used the half-filling condition $N_e = L$. This analytical value of $1/16$ is in perfect agreement with the asymptotic behavior observed in Fig. 3(b).

We further validated Eq. (S33) using Exact Diagonalization (ED) for arbitrary sets of hopping parameters $t_{1,2,3,4}$ where $p(k)$ is not constant. The numerical results show perfect agreement with our analytical derivation across all parameter regimes.

VI. A SIMPLE CONSTRAINED PATH FRAMEWORK FOR LEC-QMC

In this section, we provide a concise formulation of the constrained path (CP) realization within the LEC-QMC framework. The introduction of the constrained path approximation extends the applicability of LEC-QMC to arbitrary parameter regimes by bypassing the sign problem, while fully preserving its linear scaling complexity. The framework we proposed is a combination of the CP approximations in PQMC and FT-DQMC [S5, S6].

A. Two-Stage Sampling Scheme

We consider the Hubbard model as an example,

$$H = -t \sum_{\langle i,j \rangle, \sigma} (c_{i\sigma}^\dagger c_{j\sigma} + \text{h.c.}) + U \sum_i n_{i\uparrow} n_{i\downarrow}. \quad (\text{S36})$$

The canonical partition function for N_e fermions is written as:

$$Z = \text{Tr} \left(e^{-\beta \hat{H}} \right) = \sum_{\eta} \langle \eta | e^{-\beta \hat{H}} | \eta \rangle. \quad (\text{S37})$$

To circumvent the sign problem without performing an explicit summation over all Fock states η , we introduce a reweighting procedure based on the trial Hamiltonian \hat{H}_0 . Defining the trial weight as $W_T(\eta) = \langle \eta | e^{-\beta \hat{H}_0} | \eta \rangle$, we rewrite the partition function as:

$$Z = \sum_{\eta} W_T(\eta) \times \left[\frac{\langle \eta | e^{-\beta \hat{H}} | \eta \rangle}{\langle \eta | e^{-\beta \hat{H}_0} | \eta \rangle} \right]. \quad (\text{S38})$$

By applying the Hubbard-Stratonovich (HS) transformation to the interaction term, the quantity in the brackets can be expressed as a path integral over the auxiliary fields \mathbf{s} :

$$\mathcal{R}(\eta) = \frac{\int \mathcal{D}\mathbf{s} P(\mathbf{s}) \langle \eta | \hat{U}(\mathbf{s}) | \eta \rangle}{\langle \eta | e^{-\beta \hat{H}_0} | \eta \rangle}, \quad (\text{S39})$$

where $P(\mathbf{s})$ is a scalar factor which comes from HS transformation and depends on auxiliary fields, and $\hat{U}(\mathbf{s}) = \prod_{l=1}^M e^{-\Delta\tau \hat{H}_0} e^{-\Delta\tau \hat{H}_I(\mathbf{s}_l)}$ is the time-discretized propagator.

This decomposition justifies a two-level Markov Chain Monte Carlo approach:

1. Outer Loop (Fock State Sampling): Sample Fock states η according to the trial distribution $\mathcal{P}(\eta) \propto W_T(\eta) = \langle \eta | e^{-\beta \hat{H}_0} | \eta \rangle$. This is efficiently performed using the standard LEC-QMC algorithm driven by the sign problem free \hat{H}_0 .

2. Inner Loop (Auxiliary Field Sampling): For a fixed Fock state η , sample the auxiliary fields \mathbf{s} according to the weight

$$\frac{P(\mathbf{s}) \langle \eta | \hat{U}(\mathbf{s}) | \eta \rangle}{\langle \eta | e^{-\beta \hat{H}_0} | \eta \rangle}. \quad (\text{S40})$$

The constrained path approximation is applied within this loop to control the phase of the walker weights.

B. Random Walkers and Linear Scaling Updates

In the inner loop, we evaluate the integral for $\mathcal{R}(\eta)$ using a branching random walk. The ratio $\mathcal{R}(\eta)$ is factorized into a product of time-step updates:

$$\mathcal{P}_l^T = \langle \eta | e^{-(\beta - \tau_l) \hat{H}_0} \hat{U}(\mathbf{s}_{\tau_l \dots \tau_1}) | \eta \rangle, \quad (\text{S41})$$

$$\mathcal{R}(\eta) \approx \frac{\mathcal{P}_M^T}{\mathcal{P}_{M-1}^T} \frac{\mathcal{P}_{M-1}^T}{\mathcal{P}_{M-2}^T} \dots \frac{\mathcal{P}_1^T}{\mathcal{P}_0^T}. \quad (\text{S42})$$

We define a walker $|\phi_l\rangle$ at time slice τ_l as the state evolved from the initial $|\eta\rangle$ under the interacting propagator. The importance sampling is guided by the trial overlap $O_T(\tau_l)$, defined as the projection of the walker onto the backward-propagated trial state $\langle \psi(\tau_l) | = \langle \eta | e^{-(\beta - \tau_l) \hat{H}_0}$:

$$O_T(\tau_l) = \langle \psi(\tau_l) | \phi_l \rangle = \det[\Psi^\dagger(\tau_l) \Phi_l], \quad (\text{S43})$$

where Φ_l is the $N \times N_e$ matrix representation of the walker, and $\Psi^\dagger(\tau_l)$ represents the backward trial state.

To mitigate the sign problem, we enforce the phaseless approximation, requiring the walker to maintain a positive overlap with the guiding trial wavefunction. At each propagation step $l \rightarrow l + 1$, the walker's weight is updated by the real part of the overlap ratio:

$$w_{l+1} = w_l \times \max \left(0, \operatorname{Re} \left[\frac{O_T(\tau_{l+1})}{O_T(\tau_l)} \right] \right). \quad (\text{S44})$$

Walkers with non-positive effective weights are discarded. This constraint effectively truncates paths that cross the nodal surface defined by \hat{H}_0 .

To preserve the $O(N)$ linear scaling of LEC-QMC while minimizing variance, we perform auxiliary field updates site-by-site. This sequential strategy is essential because the optimal sampling probability for site $i + 1$ depends on the walker's configuration updated at site i .

The update of the auxiliary field s_i at site i involves applying a local operator $e^{-\Delta\tau\hat{H}_I(s_i)}$, which induces a rank-1 update to the walker matrix Φ :

$$\Phi' = (1 + \Delta_i)\Phi, \quad (\text{S45})$$

$$r = \frac{\det(\Psi^\dagger(1 + \Delta_i)\Phi)}{\det(\Psi^\dagger\Phi)}. \quad (\text{S46})$$

For numerical stability, we perform QR decompositions on both the backward trial state matrix $\Psi^\dagger = D_L U_L^\dagger$ and the walker matrix $\Phi = U_R D_R$, where $U_{L/R}$ are unitary matrices and $D_{L/R}$ are upper-triangular. The large scales in $D_{L/R}$ cancel out in the ratio, leaving only the well-conditioned unitary components:

$$r = \frac{\det(D_L U_L^\dagger(1 + \Delta_i)U_R D_R)}{\det(D_L U_L^\dagger U_R D_R)} = \frac{\det(U_L^\dagger(1 + \Delta_i)U_R)}{\det(U_L^\dagger U_R)}. \quad (\text{S47})$$

This formulation allows the ratio r and the matrix updates to be computed efficiently using the Sherman-Morrison formula. Consequently, the computational cost per sweep scales linearly with system size, consistent with the standard LEC-QMC.

We note that while advanced techniques such as force bias or heat-bath importance sampling are compatible with this framework, we present the simplest realization here to demonstrate the core methodology.

- [S1] G. H. Golub and C. F. Van Loan, *Matrix Computations*, fourth edition ed., Johns Hopkins Studies in the Mathematical Sciences (The Johns Hopkins University Press, Baltimore, 2013).
- [S2] D. Călugăru, A. Chew, L. Elcoro, Y. Xu, N. Regnault, Z.-D. Song, and B. A. Bernevig, General construction and topological classification of crystalline flat bands, *Nature Physics* **18**, 185 (2022).
- [S3] A. Mielke and H. Tasaki, Ferromagnetism in the Hubbard model: Examples from models with degenerate single-electron ground states, *Communications in mathematical physics* **158**, 341 (1993).
- [S4] H. Tasaki, From Nagaoka's ferromagnetism to flat-band ferromagnetism and beyond: An introduction to ferromagnetism in the Hubbard model, *Progress of theoretical physics* **99**, 489 (1998).
- [S5] S. Zhang, J. Carlson, and J. E. Gubernatis, A Constrained Path Monte Carlo Method for Fermion Ground States, *Physical Review B* **55**, 7464 (1997).
- [S6] Y.-Y. He, M. Qin, H. Shi, Z.-Y. Lu, and S. Zhang, Finite-temperature auxiliary-field quantum Monte Carlo: Self-consistent constraint and systematic approach to low temperatures, *Physical Review B* **99**, 045108 (2019).